Eurographics Workshop on Visual Computing for Biology and Medicine (2015)
K. Bühler, L. Linsen, and N. W. John (Editors)

Histology-Based Evaluation of Optical Coherence Tomographic Characteristics of the Cerebral Artery Wall via Virtual Inflating

S. Glaßer[1], T. Hoffmann[2], A. Boese[3], S. Voß[4], T. Kalinski[5], M. Skalej[2] and B. Preim[1]

[1] Department of Simulation and Graphics, Otto-von-Guericke University, Magdeburg, Germany
[2] Institute of Neuroradiology, Otto-von-Guericke University, Magdeburg, Germany
[3] Department of Medical Engineering, Otto-von-Guericke University, Magdeburg, Germany
[4] Department of Fluid Dynamics and Technical Flows, Otto-von-Guericke-University Magdeburg, Germany
[5] Institute of Pathology, Otto-von-Guericke University, Magdeburg, Germany

Abstract

With an increased rate of cerebrovascular diseases, the need for an advanced vessel wall analysis increases as well. In this work, we provide new information of cerebral artery walls extracted with optical coherence tomography (OCT) ex vivo. We present first results of cerebral vessel wall characteristics combined with histological image data. As a prerequisite for this combination, a new image processing method called virtual inflation *was developed. This method accounts for the missing blood pressure causing collapsing of the vessels as well as geometrical shape deformations due to catheter probing and histological imaging. We sample the vessel wall thickness locally based on the (deflated) vessel-lumen border instead of the vessel's centerline. The virtual inflation allows for co-aligning of the different image modalities. It is embedded in a multiple coordinated view framework where correspondences between the data can be highlighted via brushing and linking. In combination with histologic image data, we provide OCT signal characteristics of the human cerebral artery wall.*

Categories and Subject Descriptors (according to ACM CCS): Computer Graphics [I.3.3]: Display Algorithms—

1. Introduction

Cerebrovascular diseases are amongst the most common causes of death in the Western civilized countries. Medical imaging usually acquires the contrast-enhanced vessel lumen providing information about possible vessel stenoses or pathologies like cerebral aneurysms. However, the disease is often manifested in the vessel wall causing a pathologic weakening or thickening including atherosclerotic plaque deposits.

With an increased rate of cerebrovascular diseases, the need for an advanced vessel wall analysis increases as well. For clinical research, intravascular imaging provides new insight into the morphology of the wall and possible pathologic changes. Intravascular imaging, like intravascular ultrasound (IVUS) and recently optical coherence tomography (OCT), is employed in clinical routine for cardiology to assess stenoses and plaques due to its superior image resolution compared to tomographic imaging. An adequate imaging modality for cerebral pathologic vessel wall changes is still missing. This is due to restrictions of the medical board, i.e., the catheters might be not small and flexible enough to guarantee a safe use in cerebral vessels in vivo.

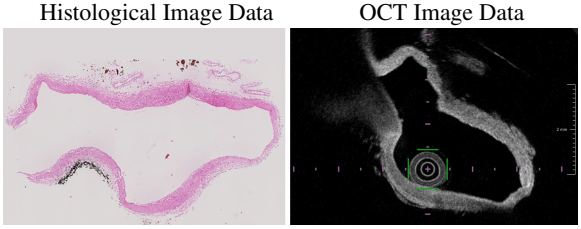

Figure 1: *Ex vivo histology and OCT slice depicting the same vessel part with varying shapes due to deflating.*

DOI: 10.2312/vcbm.20151218

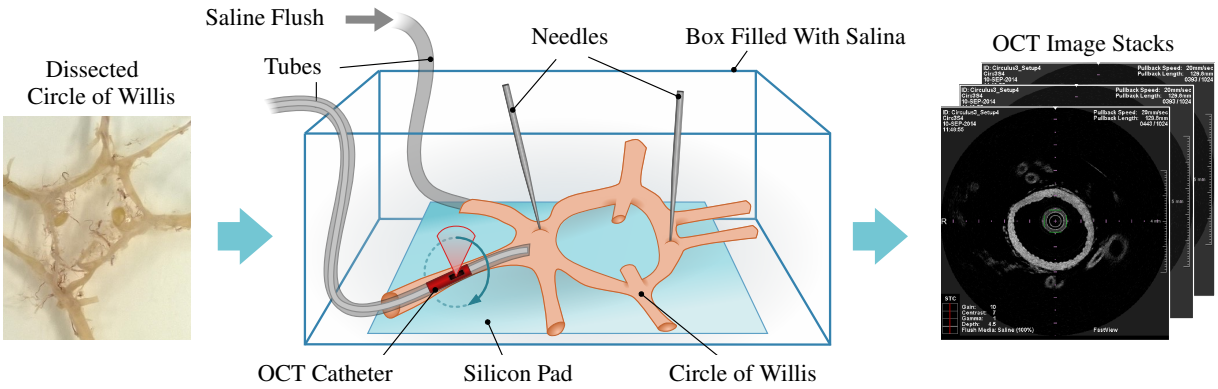

Figure 2: *Illustration of the intravascular OCT image acquisition based on the post mortem dissected Circle Of Willis preparation yielding the 2D OCT image stacks.*

For the larger carotid arteries, OCT was successfully employed to characterize atherosclerotic plaque [YKY*12]. To assess their potential for the cerebral vasculature, OCT studies have been carried out ex vivo or in animal studies [MSH*11]. Due to its ability to characterize pathological vessel wall changes and its spatial resolution superior to other intravascular imaging methods [TMF*12], it is expected that OCT imaging of the cerebral vessels will be employed and allowed for interventional use in the near future.

In this paper, we want to correlate the characteristics of OCT imaging containing cerebral plaque with histologic imaging. Our work provides basic information for the radiologic evaluation of OCT signal characteristics which are almost unknown for cerebral artery walls. To achieve this, we acquire OCT data and histology data and combine them via virtual inflation, a landmark-based approach for co-registration of the different image modalities. When it comes to ex vivo imaging of complex vasculature like the intracranial Circle of Willis, the lack of an intact blood cycle causes a deflation or collapse of vessels, see Fig. 1. Further changes of the vessel shape are caused by the ex vivo catheter probing during OCT imaging (small vessels are reshaped due to the catheter's size and stiffness) and by the sectioning of the preparations for histologic imaging.

We developed a multiple coordinated view framework for the interactive exploration of OCT and histology data. We tested our framework with a virtual model based on structure simulation deformation. We then combine atherosclerotic plaque characteristics via brushing and linking with the histologic properties and present these novel findings.

2. Related Work

Analysis of the arterial wall based on intravascular imaging is mainly carried out in cardiology. The inspiring work of Katouzian et al. [KKL*12, KKS*12] correlates intravascular ultrasound (IVUS) with histological imaging. They created a cage fixture setup for an in vitro experiment. Also for an application in cardiology, Balzani et al. [BBB*12] introduced a 3D reconstruction of geometrical models of atherosclerotic arteries (i.e., vessel walls with atherosclerotic plaque burden) based on multimodal image acquisition including IVUS, virtual histology data and angiographic X-ray images. The reconstructed 3D model comprises the inner and outer wall. The outer wall was transparently rendered and parameter values describing stress distributions were color-coded on the surface of the inner vessel wall. The visualization was combined with cross sections showing the virtual histology data. In contrast to these works, we are focusing on cerebral arteries. Thus, we are limited to the smaller vessels of the Circle of Willis including many and particularly small vessel bifurcations. During the ex vivo imaging, we cannot close all of these bifurcations leading to the problem of deflated vessels.

Regarding the research area of cerebrovascular diseases, including cerebral aneurysms, the analysis and the visualization of the cerebral vessel wall is a novel research area, mainly motivated by intravascular imaging. Glaßer et al. [GLH*14] analyzed an artificially generated porcine aneurysm, providing a visual representation of hemodynamic information as well as the wall thickness.

Related to our analysis of the cerebral vessel wall, the curvicircular feature aggregation by Mistelbauer et al. [MMV*13] samples information around the vessel's centerline to provide pathologic changes of blood vessels as an alternative to the curved planar reformation technique [KFW*02]. Their curvicircular feature technique allows for an expressive visualization of vessels and highlights stenoses. Born et al. [BSR*14] presented the 2D stent map for aortic valve stenosis analysis, where generalized cylindric coordinates are extracted from the vessel centerline to

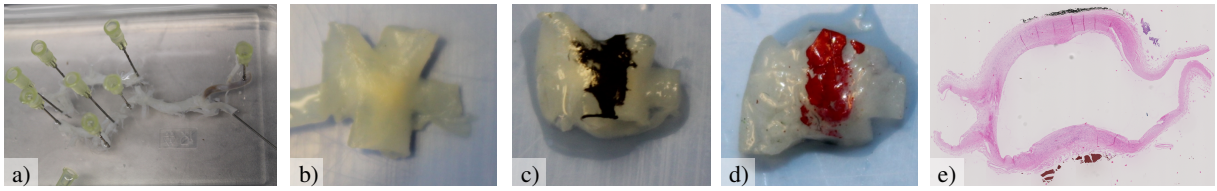

Figure 3: *Illustration of a specimen (b), taken from a Circle of Willis (a). Black and red ink is employed for later co-registration with OCT data (c-d). Final slice of the histological dataset is depicted in (e), where the red and black ink is still visible.*

create a mapping of different stent parameters, e.g., radial force or compression level. In contrast to these approaches, we do not sample around the vessel's centerline but rather along the inner vessel wall, since their work is based on in vivo CT (angiography) imaging without deflated vessels.

Similar to our work, virtual inflation can be carried out to organic tissue instead of blood vessels. These approaches are usually developed for endoscopic views, where a virtual endoscopic view is generated from a tomographic image dataset. Bartrolí et al. introduced a framework for the virtual colon unfolding [BWKG01]. They employ nonlinear ray casting and a nonlinear 2D scaling algorithm. The latter compensates distortions due to the unfolding of the colon similar to the nonlinear magnification fields used in information visualization. We developed the virtual inflation method to overcome the limitations of collapsing vessels, which is distantly related to the active contour and the balloon force concept [Coh91]. However, the active contour is allowed to move, i.e., it is attracted towards features such as edges. Our approach assumes a fixed length of the contour.

In this paper, we focus on the preprocessing of the vessel wall rather than on an automatic segmentation of the vessel walls in intravascular imaging. For larger datasets, an automatic extraction can be adapted as described in [TSDS*11].

Our framework basically employs two synchronized views of the cerebral vessels stemming from different image modalities yielding a multiple view framework. Multiple view frameworks are often employed in medical visualization and analysis, but often comprise more functionalities than our method [GRW*00]. However, we also employ brushing and linking, a concept that was initially developed for highlighting data in scatterplots [BC87]. In our framework, brushing and linking refers to the connection of different views from the different data modalities such that a change of the representation in one view affects the representation in the other.

3. Material and Methods

In this section, we discuss the requirements for the extraction of histology-based characterization of OCT-imaged vessel walls. Next, the OCT and histology image data acquisition is presented. Afterwards, the virtual inflation method is described. Finally, we introduce our framework.

3.1. Requirement Analysis

Co-registration of deflated vessels from tomographic or intravascular images with histology images is a challenging approach due to the geometrical deformation of the examined vessels. Normally, the whole image setup is adjusted such that identical portions of the data without geometrical deformations are fixed and histologic image acquisition is carried out on these fixated preparations. However, with OCT imaging, the fixation is not possible. Another option is the intravascular imaging where vessel deflation is prevented by a flush of saline solution or blood flow. This is applicable for vessel parts with only a few bifurcations but not for the arteries of the Circle of Willis that exhibit many particularly small branchings.

To cope with the ex vivo imaging and the deflation of vessels, the following requirements have to be met:

- For a better image analysis, the clinician should be able to virtually reduce the deflation of the vessel via virtual inflation.
- The virtual inflation should provide wall thickness information.
- Two virtually inflated images from corresponding vessel parts in different image modalities should be aligned.
- For the exploration of OCT images a synchronized view with histology images should be achieved.

If the required technique is available, it can be employed to extract (ex vivo) cerebral vessel wall characteristics based on OCT images providing important information about pathologic changes and their influence on cerebrovascular diseases.

3.2. OCT Image Acquisition

The experimental setup for OCT image acquisition is illustrated in Fig. 2. To check the ability of OCT to assess and characterize vascular wall structures, three human Circle of Willis were explanted post mortem. All investigations were performed in accordance with the local ethics committee.

The specimens were investigated for pathological changes of the vessel wall, e.g., plaque and aneurysms.

They were flushed with isotonic saline solution. For image acquisition, the preparations were fixated with needles on a silicon pad in a container filled with saline solution. OCT acquisition was carried out with a TERUMO LUNAWAVE^{TM} console (Terumo Corporation, Shibuya, Japan). The system is equipped with a near infrared laser light source in the spectral domain. The OCT system's pullback speed was 20 mm/s over an average distance of 130 mm yielding 1024 slices with a pixel size of 15 $\mu m \times 15$ μm. A TERUMO Fastview^{TM} 2.6 F catheter was used for all measurements.

During image acquisition, a constant saline flush of the Circle of Willis was started with an injector system. It reduced the deflation of the vessels, but it could not be prevented completely due to small outlets of the circle. Since only parts of the Circle of Willis could be acquired with one setup, i.e., with one placement of the OCT catheter, different OCT imaging setups were carried out for each preparation. As a result, we obtain a set of OCT image series for each vessel part of the Circle that exhibits vessel diameters large enough for catheter probing. A detailed explanation of the OCT imaging setup can be found in [HGB*15].

3.3. Histology Acquisition

For histologic evaluation, certain parts of the vessels with atherosclerotic plaque and prominent bifurcations (for orientation purpose) were selected, see Fig. 3. Additionally, the specimen was marked lengthwise doublesided with black and red ink. After paraffin embedding, cross sections of the specimen were cutted using a microtome with a thickness of 2 μm and a slice gap of 50 μm. The sections were transferred to standard glass slides, stained with hematoxilin and eosin (H&E) and coverslipped. The slides were digitalized using a Hamamatsu Nanozoomer (Hamamatsu, Japan) with a resolution of .23 μm per pixel. The original proprietary file was formatted to JPEG2000 [KZS*08].

The digitalized slices were then stacked into a volume for the processing with our framework. For easy handling of the high-resolution data, we downsample the data to 25%, yielding a reduction from 20.480 $\times$ 14.080 pixels to 5.120 $\times$ 3520 pixel with a resolution of .92 μm per pixel. The reduction enables a fast image processing without loss of important information since the nuclei which are important for plaque evaluation can still be determined, see Fig. 4.

3.4. Virtual Inflation

Our virtual inflation method to inflate the collapsed or deflated vessels is illustrated in Fig. 5. The virtual inflation method can be employed for OCT and histology data. It only requires the contours of the walls. Initially, we manually extracted the contours of the vessel-lumen, i.e., the inner wall,

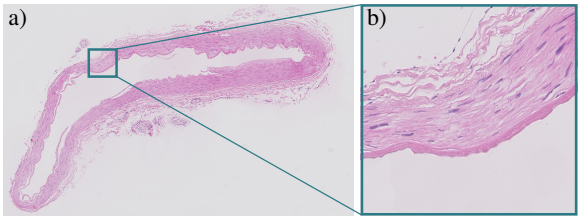

Figure 4: *In a), the JPEG2000 file is depicted. The inlet in b) shows blue nuclei at a reduced image with a resolution of .92 μm.*

and the vessel-surrounding border, i.e., the outer wall (recall Fig. 5a). The segmented contours are converted into equidistantly sampled line segments (see Fig. 5b):

1. A point cloud from all contour points was extracted.
2. The points were sorted in a list. Based on an arbitrary starting point the closest point was added to the list and its next closest, yet not visited point was added until all points were added.
3. The list of points was equidistantly sampled (the user can change the amount of sampling points, the default, empirically determined, values are 400 sampling points for an OCT slice with 600 $\times$ 600 pixels and 1600 sampling points for an histology slice with approx. 5000 $\times$ 3500).
4. The equidistantly sampled points list was smoothed via linear interpolation.
5. The final line segments must be arranged clockwise around the vessel center m. Otherwise, we flipped the list of points.

The clockwise arrangement of line segments is necessary for our multiple linked view framework for the successful co-alignment of both viewed datasets. We then traveled along the inner contour and extracted a normal $\overrightarrow{n}$ for each contour point p perpendicular to the straight line spanned between its predecessor and successor (see Fig. 5c). We approximated the wall thickness t at p as distance to the vessel-surrounding border, i.e., t was extracted with the intersection between a ray from p in direction $\overrightarrow{n}$.

Finally, we transformed the vessel-lumen border contour into a circle with the same center m and with radius r with $r = c/(2\pi)$, where c is the circumference of the vessel-lumen border (see Fig. 5e). We remodeled the vessel-surrounding border by adding the previously extracted t values to each point p' of the circle in direction $\overrightarrow{mp}'$ (the ray from the circle's center m through p'). Connecting the approximated positions yielded the vessel-lumen border.

Thus, we obtained the virtually inflated vessel. With linear interpolation, we could create intermediate steps of the virtually inflated vessel, e.g., we translated the point p only half the distance between p and its corresponding point p' of the virtually inflated circular vessel-lumen border (see Fig. 5f).

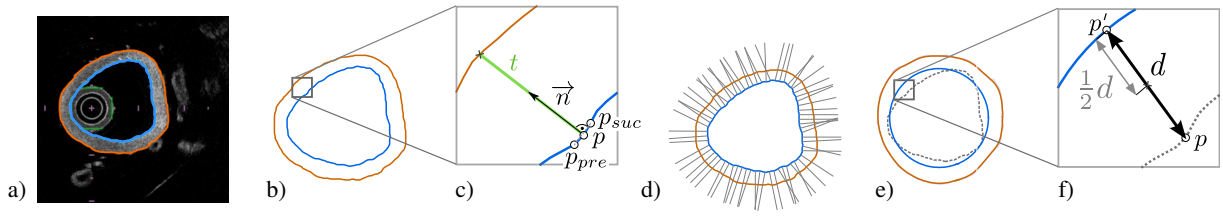

Figure 5: *Illustration of the virtual inflation. In the original image, the inner (orange) and the outer (blue) vessel wall was segmented (a). A normal n was extracted and the wall thickness t was measured (see b and c) for each point of the inner surface (d). Afterwards, the vessel-lumen border is transformed into a circle with corresponding wall thickness (e). Intermediate points are obtained via linear interpolation (f).*

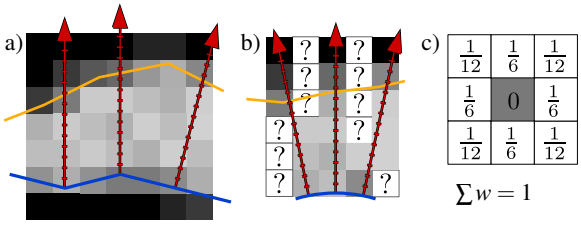

Figure 6: *Sampling of intensity values. a) The original image with the two contours (orange and blue). b) The samples are accumulated along the rays (red) to interpolate the pixels' values in the transformed image. c) If no sample value was assigned to a pixel, its intensity (at the center) is interpolated with the depicted filter kernel.*

We subsampled the rays constructed from the vessel-lumen border pointing at the vessel-surrounding border to translate the intensity values of the original image to the virtually inflated image (see Fig. 6). We empirically set the step size for the sample to 0.2 of the voxel's width. We acquire for each pixel of the virtual inflated images a list of samples (if k rays cover the pixel, then k samples are obtained) and interpolated the pixel's intensity by averaging over the samples. If a pixel x with no samples exists, the pixel's intensity value $I(x)$ is interpolated from its neighborhood N (see Fig. 6c):

$$I(x) = \sum_{q}^{q \in N} \frac{1}{w_q} * I(q). \quad (1)$$

If more than one pixel is missing, the sum of weights $\sum w$ drops below 1. In this case, we left the missing pixels out and multiply the sum of the remaining pixels with $(\sum w)^{-1}$.

To exploit as many samples as possible, we first created a ranking of the pixels, where we counted the number of missing neighbors. Then, we interpolated all pixels with one neighbor missing, followed by pixels with two neighbors missing and so on. The interpolation was only carried out for pixels surrounded by the two vessel borders in the final image.

The virtual inflation of the vessel wall can be linearly interpolated by extracting the intermediate positions of the points of the inner wall (recall Fig. 5f) and the intermediate contour of the vessel-lumen border is obtained. Then, the sampled intensities are translated to the intermediate images as well. Again, the normal $\vec{n}$ for each intermediate contour point p was extracted as perpendicular vector from the straight line spanned between $p's$ predecessor and successor. The linearly interpolated virtual inflation is presented in Fig. 7 and allows the clinical expert an interactive inflation and exploration of the data.

3.5. Framework

We created a multiple coordinated view framework in MATLAB (Product of MathWorks, Natick, USA) for the interactive exploration of the datasets, see Fig. 8. The framework simultaneously shows an OCT view and a histology view. Both datasets are linked based on their world coordinate system. The initial correlation of the vessel slices is realized landmark-based, e.g., with the selection of a bifurcation. If the user scrolls to a slice in one of the views, the other view is updated accordingly. Next, the virtual inflation is separately carried out for both views and the user can qualitatively explore the vessel wall and choose between different interpolation steps, see Fig. 7. Thus, the clinician does not have to interpret the virtually inflated images, but can still improve the visual representation by choosing a step in between.

For the interactive exploration, we included brushing and linking. The artificial circular cross section, i.e., the virtual inflation, forms the basis for interactively brushing and linking, see Fig. 9. The user selects a set of points forming a polygonal region of interest (ROI) - the brush. This brush is translated for each interpolation step of the virtual inflation. Finally, a correlation between a possible brush from the virtually inflated OCT image to the virtually inflated histology image (or vice versa) is carried out. As a prerequisite, the user selects two corresponding landmarks on the inner vessel wall of the virtually inflated images, e.g. the small vessels (see cyan circles) in Fig. 9. Then, the brush from the virtually inflated histology image is translated to the original

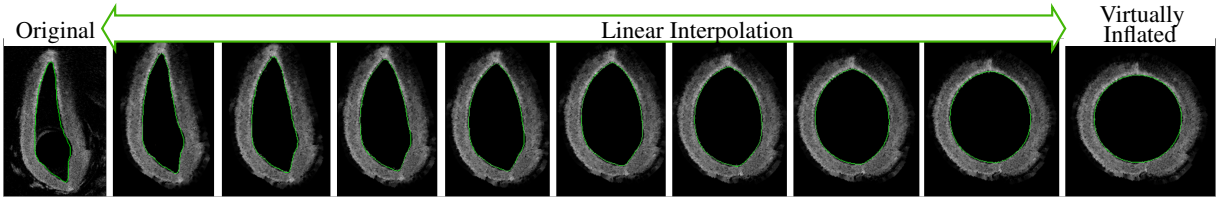

Figure 7: *Result of the virtual inflation method and combined sampling of intensity values applied to a deflated vessel OCT cross-section view. Intermediate steps are created via linear interpolation of the positions of the inner vessel wall points.*

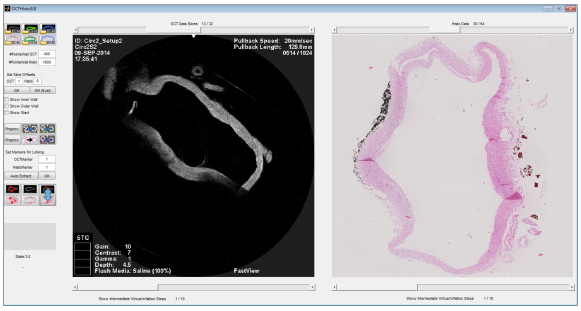

Figure 8: *Screenshot of the graphical user interface of our framework depicting an OCT image data (left) and a histology image data (right).*

histology image. Thus, a ROI can be defined in the original OCT image and will be linked to its corresponding ROI in the original histology image. The brush can also be defined in the histology image first and linked to the OCT image afterwards. The clinician can correlate the image characteristics of a specific part in the OCT image with the histology image and vice versa. Hence, the evaluation should primarily be carried out in the original images, and the virtually inflated images improve wall thickness estimation and allow for brushing and linking.

The exploration as well as the brushing and linking can be carried out interactively. The runtime of the virtual inflation step depends on the number of intermediate images. For the presented OCT data, the sampled intensities are extracted in 0.47 s. Creation of the single virtually inflated circular cross section from the sampled intensities costs approx. 3.7 s whereas the creation of 10 intermediate images costs approx. 35.4 s on a desktop pc with 8 GB RAM and a Intel(R) Core i5 CPU (3.20 GHz). Source code is provided at the project's website: `http://www.forschungscampus-stimulate.de/en/research/resources/virtualinflation/`.

4. Evaluation

Our method is especially tailored to deflated vessels in two different image modalities. Due to the novelty of the presented medical application, a ground truth is not available. To overcome this limitation, we designed a software-based approach which provides two vessel deformations and serves as ground truth to assess the accuracy of our method. The deformation of the software phantom is realized via different finite-element simulations yielding information about the deformation as well as the detailed position of random points before and after the deformation.

The finite-element method is widely used to numerically calculate the relation of deformation, mechanical strain and mechanical stress, respectively, based on the conversation of the momentum, which is solved locally for each finite element. Based on this, we can conduct an evaluation taking into account the physical material behavior in combination with known locations of each discrete element. The static simulations considering large deflections and small strains were carried out on a standard personal computer using the software ANSYS Mechanical (ANSYS, Inc., Canonsburg, USA).

The dimensions of the 2D model of a simplified vessel cross section are carefully matched to the properties of cerebral vessels with an outer radius of 2.5 mm and an inner radius of 2.2 mm, respectively. In addition, two local wall thickenings of 0.2 mm are present at the inside, see Fig. 10. Furthermore, the outer wall exhibits two corners. These characteristics serve as anatomical landmarks for the subsequent virtual inflation step. The numerical model consists of ca. 77.000 tetrahedral elements with quadratic basis function to obtain high accuracy. This results in a typical element edge size of 15 μm. To induce deformation, a load is applied as body force (similar to the weight force) in positive y-coordinate direction, yielding the software phantom P_1, and negative y-coordinate direction, yielding the software phantom P_2. The body force influences all tetrahedral elements. Rigid body motion is prevented by fixating the displacement in y-direction at the bottom edge and additionally in x-direction at the bottom right vertex. The load causes mechanical stress in the model's inside and results in deformation depending on the specified linear elastic material model. The Young's modulus is 1 MPa, the Poisson's ratio is 0.45 and the density is 1000 kg/m^3, as employed in [BHZ*10] to investigate the movement of cerebral vessel walls.

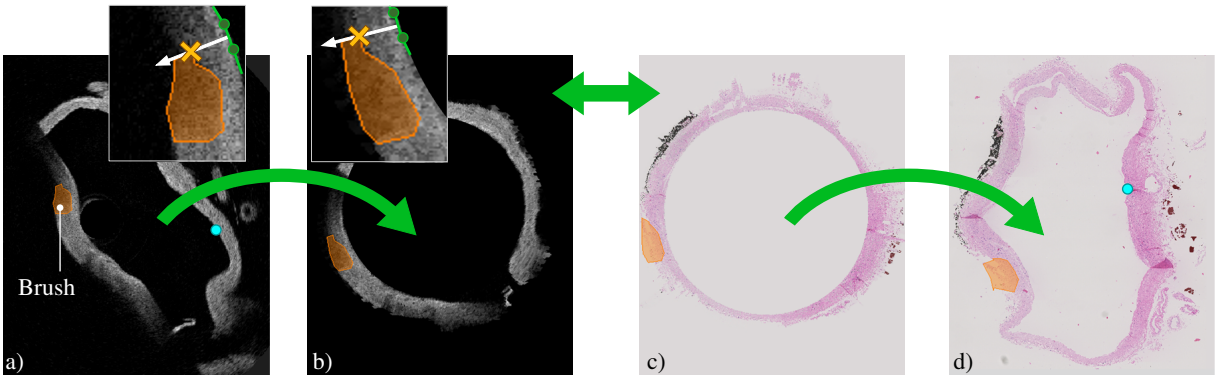

Figure 9: *Illustration of the brushing and linking. Corresponding OCT and histology slices and their virtually inflated images are depicted. When the user defines a brush (a), it is automatically converted to the inflated view (b) based on the distance of the vertices of the brush and their distance to the vessel-lumen border (see inlets). The virtually inflated images of OCT and histology can be correlated, (b) and (c). Analogously, the brush can be translated from the inflated to the original image (d).*

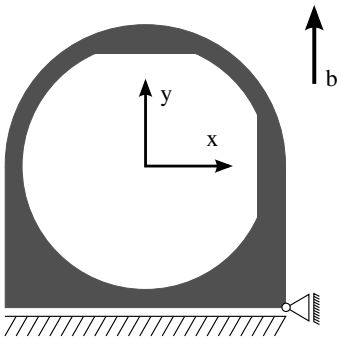

Figure 10: *Software phantom in initial, stress-free state. The local coordinate system is placed in the center of the 2D geometry. The load is applied as body force b, while the bottom is fixated to prevent rigid body motion.*

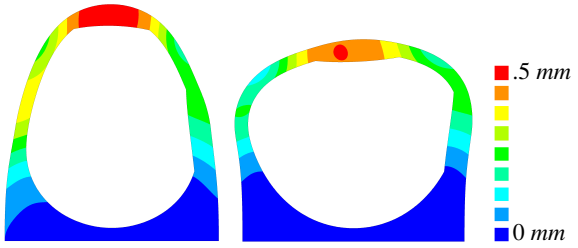

Figure 11: *Contour plot of the vector displacement for P_1 (left) and P_2 (right).*

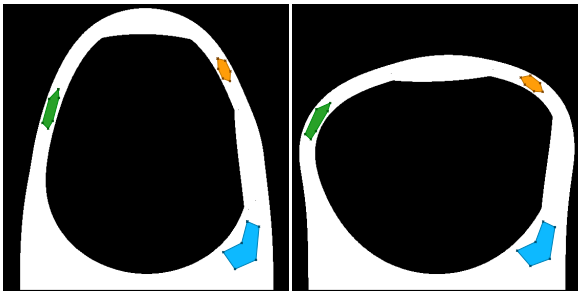

Figure 12: *Depiction of the binarized images I_1 and I_2 and three different brushes placed in I_1. Via virtual inflation, a linking of the brushes to I_2 was carried out.*

Deformation resulting from the described load is shown in Fig. 11. The vector displacement ranges up to .5 *mm*. Finally, coordinates and displacements of approx. 156.000 vertices are stored in the software phantoms P_1 and P_2. We employ the displacements as ground truth.

Next, we converted the software phantoms P_1 and P_2 with MATLAB into two binary images I_1 and I_2 and stored them as DICOM data for further processing with our method. Hence, we employ an image size of 600×700 pixel where 1 pixel covers .01 *mm* $\times$ .01 *mm*. We extract for each point of P_1 and P_2 its pixel position by translating the coordinate system origin in the bottom left corner yielding the binary images presented in Fig 12. We then load the two images into our software tool and define three brushes as hexagons. Through linking, the brush of image I_1 was transferred to I_2 and we store the pixel coordinates of the transferred brush.

To assess the suitability of our method, we compare the pixel coordinates of the corresponding brushes obtained via linking the (ground truth) displacement from P_1 to P_2. Therefore, we carry out the following transformation for each brush B_1, B_2, and B_3:

1. Extract the pixel coordinates for the six vertices of $B_{1..3}$ from I_1.
2. Select the corresponding world coordinates of P_1, i.e., transpose the pixel coordinates into world coordinates.
3. Derive the corresponding world coordinates of these points in P_2 (know from the finite-element simulation).
4. Convert the points from P_2 into pixel coordinates of I_2.
5. Compare the pixel coordinates with the pixel coordinates from I_2 extracted via linking.

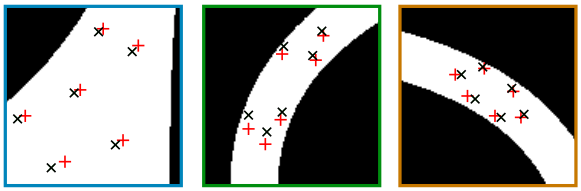

\+ Position extracted with virtual inflation
× Position extracted from software phantom

Figure 13: *Depiction of the variations of the automatically determined brush positions via virtual inflation and the positions extracted from the software phantoms. The color of the box is assigned w.r.t Fig. 12.*

The variations of the brushes B_1-B_3 are illustrated in Fig. 13. Now, we can calculate the differences from the distances compared to the ground truth displacements yielding the results presented in Tab. 1. The average displacement is approx. 49.4 μm.

Furthermore, we create a random point set of 100 points that were randomly placed at the foreground object in I_1. Then, we extract their corresponding positions in I_2. The resulting average displacement of 48.9 μm equals the average displacement for the brushes B_1-B_3.

As a result, the differences between the ground truth displacement and transferred brush via linking are fairly small. In relation to the image size of 600 × 700 pixels, the displacement of approx. 5 pixels equals 0.71 % - 0.83 %. Although the small displacement rate depends on the perfectly matched software phantom and may differ for real preparations, the virtual inflation allows for linking of a defined brush in one image to the other image.

5. Medical Findings

Our database contains data sets which were probed ex vivo. Thus, a detachment of the intima, i.e., the inner vessel wall which can be found at the vessel-lumen border, emerged. This typically occurs during decomposition since the data was examined ex vivo. We carried out virtual inflation of portions of the data, including the branching basilar artery with artherosclerotic plaque. Hence, we do not intend to use the virtual inflation for reliable image characteristics but for the visual representation and correlation of OCT and histology. We discussed the results with a neuroradiologist and a pathologist. In Fig. 14, we provide an overview of the most important characteristics and results.

	Distances [μm]						
	d_1	d_2	d_3	d_4	d_5	d_6	$\overline{d}$
B_1	36.5	43.1	51.4	10.1	60.2	55.4	57.9
B_2	33.8	50.4	83.3	82.9	49.7	34.1	55.7
B_3	40.2	58.6	44.1	26.2	25.9	12.6	34.6
Overall average displacement:							49.4

Table 1: *Euclidean distances between the transferred brushes B_1, B_2, and B_3 via virtual inflation and the exact positions based on the software phantoms. Distances are based on pixel positions and 1 pixel covers 10 μm × 10 μm.*

In Fig. 14(a), the histologic evaluation revealed a fibrotic plaque deposit in the intima, i.e., a thickening of the inner vessel-lumen border. When brushing the fibrotic deposits, the linking to the OCT slice reveals an area with dense plaque accumulation, see the dense tissue parts with high attenuation (marked with *) yielding the low attenuated areas behind. In Fig. 14(b), an accumulation of mucoid plaque was brushed. This tissue is typically loose. As it can be seen in the OCT image, the brushed region is part of the plaque area with low signal and low attenuation, but no specific differences can be extracted. In Fig. 14c), a small area with inflammatory cells (which are characterized by sharp, round cell nuclei) was selected. Inflammations often vary and a precise prediction concerning their density values is not possible. This is reflected in the small brush in the OCT image (Fig. 14(c) right), which reveals a small, heterogeneous area. The last example in Fig. 14(d) covers a part of the vessel wall which was suspicious during histology evaluation. Hence, a thickening of the vessel wall may be observed. However, detailed analysis of the histologic image does not confirm a plaque deposit. Instead, an accumulation of non-pathologic cells was identified. This finding is confirmed with the OCT images where no change in the signal characteristics existed.

Hence, our novel imaging of the cerebral plaque yields similar results as reported for known cases of coronary plaque in literature [YKY*06]. Although our framework lacks of handling ellipsoidal vessel cross sections, the user can vary the amount of virtual inflation via linear interpolation, recall Fig. 7. This accounts for the fact that vessels may exhibit ellipsoidal cross sections as well as various elongated cross sections due to pathologies.

6. Discussion

The proposed virtual inflation method allows a combination of OCT and histologic image modalities. The spatial differences between a brush and the corresponding brush in the second image modality were evaluated based on finite-

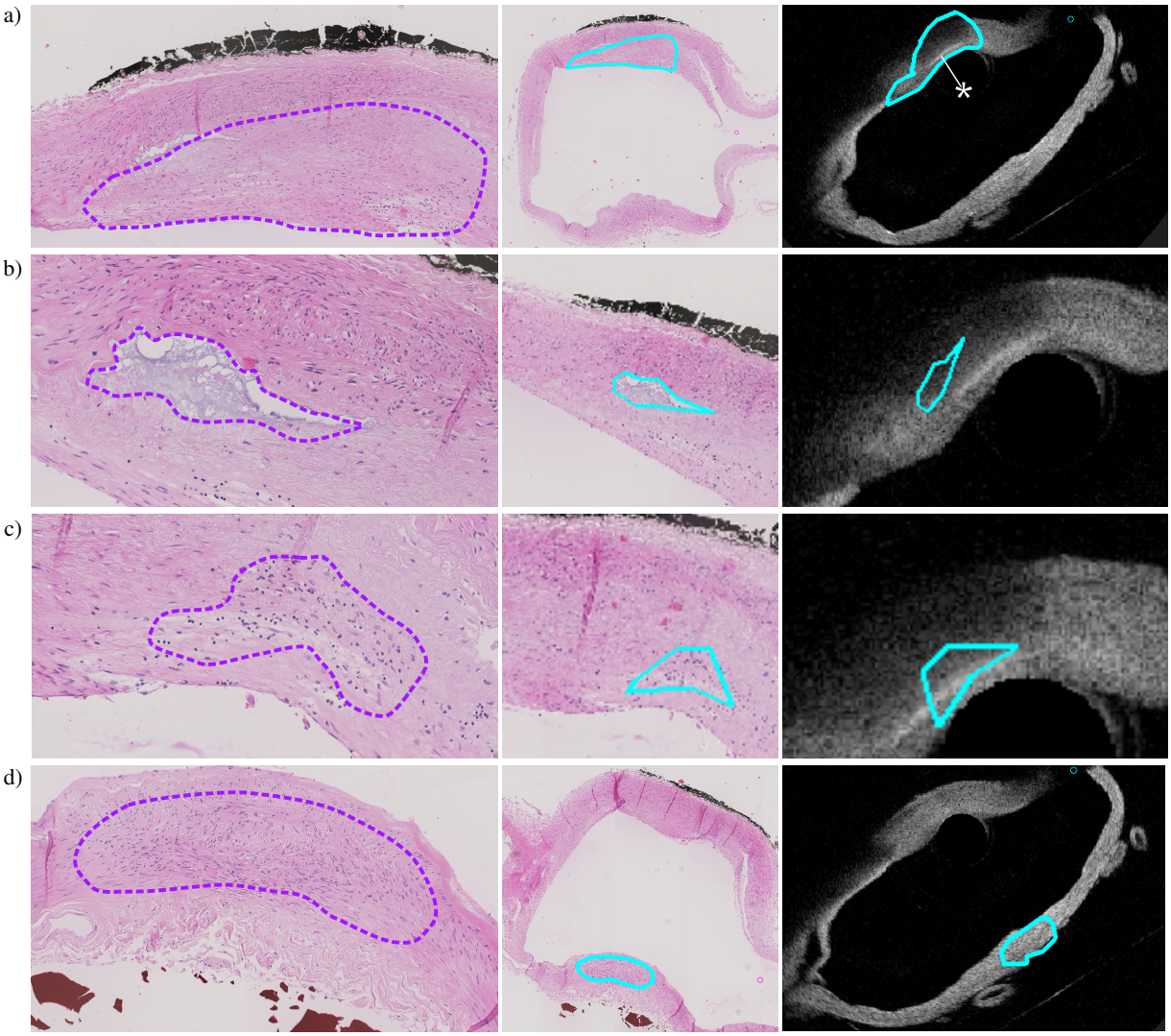

Figure 14: *Examples for the correlation of histology and OCT images. For each example a)-d), the left row represents an enlargement of the histologic image. Then, a brush was defined in the histological view and linked (via virtual inflation) to the OCT view.*

element simulations yielding a sufficient precision. For the medical image data, the in-plane precision must be evaluated in more detail, e.g., by implanting some markers like a small thread in the preparations. Naturally, a larger study can provide more information of the in-plane resolution and assess more artifacts like conservation-based shrinking. Nevertheless, the combination of the ex vivo OCT and histologic properties provides new information about the cerebral vessel wall morphology and its corresponding OCT imaging. Such findings can form the basis for a solely radiology-based OCT image interpretation and evaluation.

The sampling of the intermediate steps to transform the original vessel into the circular cross section could be improved w.r.t. intersecting rays. This problem often arises when the thickness of organs or tissue parts has to be measured, e.g., the corpus callosum [HKW12]. At the moment, the interpolation of virtual inflation only serves as additional presentation of the data.

7. Summary

In this paper, we presented a virtual inflation of ex vivo vessel parts probed with OCT and acquired with histology to analyze characteristics of the cerebral vessel wall. Our prototype requires manual segmentation of the vessel-lumen and

the vessel-surrounding borders. It is adapted to intravascular imaging of the cerebral vasculature. Our framework comprises a multiple coordinated view which allows for brushing and linking. Thus, a brush defined in the OCT image will be highlighted in the histological image view and vice versa.

Future work should account for non-circular cross sections as well as automatically segmented vessel walls, as presented in [TSDS*11]. We are particularly interested in a setup similar to the cage fixture for an in vitro experiment setup, as presented in [KKL*12, KKS*12]. However, their work is based on intravascular ultrasound, whereas OCT would require different adaptions of this environment.

Finally, our work has great importance for the numerical simulation of blood flow. The new wall information based on virtually inflated images are essential to investigate the fluid-structure interaction regarding vessel wall and blood flow. Currently, hemodynamical simulation experts are using our approach to examine the effect of wall thickness on simulation results.

Acknowledgements

This work was partly funded by the German Federal Ministry of Education and Research within the Forschungscampus STIMULATE (grant number: 13GW0095A).

References

[BBB*12] BALZANI D., BÖSE D., BRANDS D., ERBEL R., KLAWONN A., RHEINBACH O., SCHRÖDER J.: Parallel Simulation of Patient-Specific Atherosclerotic Arteries for the Enhancement of Intravascular Ultrasound Diagnostics. *Engineering Computations 29*, 8 (2012), 888–906. 2

[BC87] BECKER R. A., CLEVELAND W. S.: Brushing Scatterplots. *Technometrics 29*, 2 (1987), 127–142. 3

[BHZ*10] BAZILEVS Y., HSU M.-C., ZHANG Y., WANG W., LIANG X., KVAMSDAL T., BREKKEN R., ISAKSEN J. G.: A Fully-Coupled Fluid-Structure Interaction Simulation of Cerebral Aneurysms. *Comput Mech 46*, 1 (2010), 3–16. 6

[BSR*14] BORN S., SUNDERMANN S. H., RUSS C., HOPF R., RUIZ C. E., FALK V., GESSAT M.: Stent Maps - ŮComparative Visualization for the Prediction of Adverse Events of Transcatheter Aortic Valve Implantations. *IEEE Transactions on Visualization and Computer Graphics 20*, 12 (2014), 2704–2713. 2

[BWKG01] BARTROLÍ A. V., WEGENKITTL R., KÖNIG A., GRÖLLER E.: Nonlinear Virtual Colon Unfolding. In *Proc. of IEEE Visuslization* (2001), IEEE Computer Society, pp. 411–420. 3

[Coh91] COHEN L. D.: On Active Contour Models and Balloons. *CVGIP: Image Understanding 53*, 2 (1991), 211–218. 3

[GLH*14] GLASSER S., LAWONN K., HOFFMANN T., SKALEJ M., PREIM B.: Combined Visualization of Wall Thickness and Wall Shear Stress for the Evaluation of Aneurysms. *IEEE Transactions on Visualization and Computer Graphics (TVCG)* (2014), 2506–2515. 2

[GRW*00] GRESH D. L., ROGOWITZ B. E., WINSLOW R. L., SCOLLAN D. F., YUNG. C.: WEAVE: A System for Visually Linking 3-D and Statistical Visualizations, Applied to Cardiac Simulation and Measurement Data. In *Proc. of IEEE Visualization* (2000), pp. 489–92. 3

[HGB*15] HOFFMANN T., GLASSER S., BOESE A., BRANDSTÄDTER K., KALINSKI T., BEUING O., SKALEJ M.: Experimental Investigation of Intravascular OCT for Imaging of Intracranial Aneurysms. *International Journal of Computer Assisted Radiology and Surgery* (2015), 1–11. 4

[HKW12] HERRON T. J., KANG X., WOODS D. L.: Automated Measurement of the Human Corpus Callosum Using MRI. *PMC 25*, 6 (2012). 9

[KFW*02] KANITSAR A., FLEISCHMANN D., WEGENKITTL R., FELKEL P., GRÖLLER M. E.: CPR: Curved Planar Reformation. In *Proc. of IEEE Visualization* (2002), pp. 37–44. 2

[KKL*12] KATOUZIAN A., KARAMALIS A., LISAUSKAS J., ESLAMI A., NAVAB N.: IVUS-Histology Image Registration. In *Proc. of Biomedical Image Registration, Springer Berlin Heidelberg* (2012), pp. 141–149. 2, 10

[KKS*12] KATOUZIAN A., KARAMALIS A., SHEET D., KONOFAGOU E., BASERI B., CARLIER S. G., ESLAMI A., KONIG A., NAVAB N., LAINE A. F.: Iterative Self-Organizing Atherosclerotic Tissue Labeling in Intravascular Ultrasound Images and Comparison With Virtual Histology. *IEEE Transactions on Biomedical Engineering 59*, 11 (2012), 3039–3049. 2, 10

[KZS*08] KALINSKI T., ZWÖNITZER R., SEL S., EVERT M., GUENTHER T., HOFMANN H., BERNARDING J., ROESSNER A.: Virtual 3D Microscopy Using Multiplane Whole Slide Images in Diagnostic Pathology. *American Journal of Clinical Pathology 130*, 2 (2008), 259–264. 4

[MMV*13] MISTELBAUER G., MORAR A., VARCHOLA A., SCHERNTHANER R., BACLIJA I., KÖCHL A., KANITSAR A., BRUCKNER S., GRÖLLER E.: Vessel Visualization using Curvicircular Feature Aggregation. *Computer Graphics Forum 32*, 3pt2 (2013), 231–240. 2

[MSH*11] MATHEWS M. S., SU J., HEIDARI E., LEVY E., LINSKEY M. E., CHEN Z.: Neuroendovascular Optical Coherence Tomography Imaging and Histological Analysis. *Neurosurgery 69*, 2 (2011), 430–439. 2

[TMF*12] TSAKANIKAS V. D., MAICHALIS L. K., FOTIADIS D. I., NAKA K. K., BOURANTAS C. V.: *Intravascular Imaging: Current Applications and Research Developments*. IGI Global, 2012. 2

[TSDS*11] TUNG K.-P., SHI W.-Z., DE SILVA R., EDWARDS E., RUECKERT D.: Automatical Vessel Wall Detection in Intravascular Coronary OCT. In *Proc. of IEEE Symp. on Biomedical Imaging: From Nano to Macro* (2011), pp. 610–613. 3, 10

[YKY*06] YOSHIMURA S., KAWASAKI M., YAMADA K., ENOMOTO Y., EGASHIRA Y., HATTORI A., ET AL.: Diagnostic Accuracy of Optical Coherence Tomography and Integrated Backscatter Intravascular Ultrasound Images for Tissue Characterization of Human Coronary Plaques. *Journal of the American College of Cardiology 48*, 1 (2006), 81–88. 8

[YKY*12] YOSHIMURA S., KAWASAKI M., YAMADA K., ENOMOTO Y., EGASHIRA Y., HATTORI A., NISHIGAKI K., MINATOGUCHI S., IWAMA T.: Visualization of Internal Carotid Artery Atherosclerotic Plaques in Symptomatic and Asymptomatic Patients: A Comparison of Optical Coherence Tomography and Intravascular Ultrasound. *American Journal of Neuroradiology 33*, 2 (2012), 308–313. 2